Journal of Materials Chemistry A

Accepted Manuscript

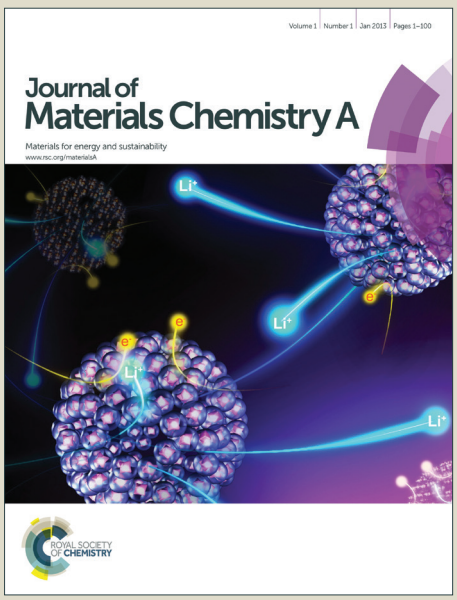

ROYAL SOCIETY OF CHEMISTRY

www.rsc.org/materialsA

ARTICLE TYPE www. rsc.org/xxxxxx | XXXXXXXX

Prediction and Characterisation of Radiation Damage in Fluorapatite

Eleanor E. Jay, Paul C.M. Fossati, Michael J.D. Rushton and Robin W. Grimes*

Received Xth XXXXXXXXXX 20XX, Accepted Xth XXXXXXXXX 20XX
First published on the web Xth XXXXXXXXXX 200X
DOI: 10.1039/b000000x

Molecular dynamics simulations, used in conjunction with a set of classical pair potentials, have been employed to examine simulated radiation damage cascades in the fluorapatite structure. Regions of damage have subsequently been assessed for their ability to recover and the effect that damage has on the important structural units defining the crystal structure, namely phosphate tetrahedra and calcium meta-prisms. Damage was considered by identifying how the phosphorous coordination environment changed during a collision cascade. This showed that PO_4 units are substantially retained, with only a very small number of under or over coordinated phosphate units being observed, even at peak radiation damage. By comparison the damaged region of the material showed a marked change in the topology of the phosphate polyhedra, which polymerised to form chains up to seven units in length. Significantly, the fluorine channels characteristic of the fluorapatite structure and defined by the structure's calcium meta-prisms stayed almost entirely intact throughout. This meant that the damaged region could be characterised as amorphous phosphate chains interlaced with regular features of the original undamaged apatite structure.

1 Introduction

Apatite is the most abundant naturally occurring phosphate mineral[1]. Due to this system's considerable compositional flexibility it is used in a number of applications[2,3]. In particular, it has been observed that a wide range of elements can be accommodated in synthetic and naturally occurring apatites[4,5]. This compositional flexibility is being exploited by the nuclear industry where apatites are being considered as constituents for multi-compound waste forms. Furthermore, apatites are known to incorporate halides and rare earth elements[2], which can be problematic for first generation waste forms such as borosilicate glasses, due to their low solubility in these materials[6–8].

The suitability of apatites for use as waste hosts, has previously been investigated via fission-track thermochronometry[9], which is widely used to measure processes occurring in the Earth's crust[10]. This approach compares the abundance of naturally-occurring radioactive isotopes and their decay products within a sample and measures the size and shape of fission tracks[11]. This has shown that apatite minerals have sucessfully immobilised radionuclides over geological time-scales making them relevant to the long term disposal of high level nuclear waste with the longevity of these materials, even under the damaging effects of self-irradiation, indicating that synthetic analogues may make suitable waste hosts. In particular, fluorapatite (FAp) is being considered as a possible waste material[5,12–14].

The thermochronometry studies of Gleadow *et al.*[9] clearly show the formation of radiation damage tracks within fluorapatite and describe the mechanism of track formation as being the combination of two coincident and brief processes: upon decomposition of an atomic nucleus, fission fragments with excess kinetic energy move in opposite directions and interact with the host lattice so that collisions between fission fragments and lattice ions lead to lattice damage. Weber *et al.*[16] suggest that both the structure of the centre of these damage tracks and the lattice immediately surrounding them is little known. However, understanding the structure of such damage, the mechanisms underlying its creation and subsequent recovery has profound implications for materials performance under repository conditions. Moreover, with improved understanding, better nuclear waste form materials could be designed. To this end molecular dynamics (MD) calculations employing effective pair potentials are used here to characterise the damage caused within the FAp lattice when exposed to displacive radiation.

A major cause of defect production within the crystalline structure of a waste material occurs when the lattice is subjected to the effects of α-decay[17]. An energetic α-particle is initially slowed through electronic stopping, as it undergoes inelastic collisions with lattice ions. This initial phase leads to the production of electronic defects and localised heating. As particles lose energy through these interactions, such that its kinetic energy drops below 100 keV, nuclear stopping pre-

Department of Materials, Imperial College London, Exhibition Road, London, SW7 2AZ, United Kingdom. Tel: +44(0)207 7594 6730; E-mail: r.grimes@imperial.ac.uk

dominates. At this point elastic collisions between the incident particle and the lattice can take place[18]. These can impart significant kinetic energy to lattice ions, referred to as primary knock-on atoms (PKAs), leading to a cascade of collisions that are likely to form point defects. It is this latter phase of the damage process that the work presented here aims to simulate.

MD is used to simulate ballistic damage cascades over a period of 100 ps, which allows the initial damage processes to be examined in some detail. Furthermore, the simulations also provide a strong mechanistic basis for understanding lattice recovery. Although a full appreciation of a waste host's performance requires material behaviour to be understood over geological timescales ($>10^5$ years)[17], the short time-scale information provided by MD does provide important insight regarding the damage imparted to the lattice by damage cascades.

Initially, the effect of crystallographic direction on the threshold displacement energies of each species in FAp will be described by using the results of MD caculations employing the primary knock-on atom method detailed in section 2. From these threshold energies the Kinchin-Pease model[19] is used to predict the point defect population obtained from high energy radiation damage cascades (section 3.1). The efficacy of the Kinchin-Pease method, as applied to FAp, is examined by comparing its predictions with the results of MD simulations of collision cascades initiated using 5 keV PKAs. In order to better understand the nature of the damage processes operating in FAp, the number and type of lattice defects obtained as a 5 keV cascade evolved through its damage and recovery phases have been characterised. Finally, the effect of the damage on the constitution of the phosphate polyhedra making up the structure is studied; in particular, the damage induced polymerisation of these units is considered with the topology of phosphate polymer chains being described.

1.1 Fluorapatite Structure

Naturally occurring apatite has the chemical formula: $A_{10}(XO_4)_6B_2$[20], where commonly, B= F, OH or Cl, A = Ca, Sr, Pb, Na etc. and X= P, As, Si, V etc.[2]. The apatite structure is hexagonal and exhibits space-group $P6_3/m$, as described by White *et al.*[21]. This consists of a central channel (first identified by Beevers and McIntyre[22]) containing a large anion, which can be Cl^-, F^- or OH^-, and is surrounded by CaO_6 and PO_4 polyhedra as corner connected units. This can be seen within figure 1 where they describe the hexagonal shape of the central channel. In the present work, the fluorapatite composition is considered, $Ca_{10}(PO_4)_6F_2$, in which F^- occupies the central channel (B site) and is surrounded by Ca in the A sites.

Fluorapatite has two distinct calcium sites, the first is a nine-fold coordinated $4f$ site, Ca(1), which forms a metaprism of two triangles on mirror planes and the second, Ca(2), is a seven-fold coordinated $6h$ site, which is linked with phosphate groups and a channel anion, forming a hexagonal network[20].

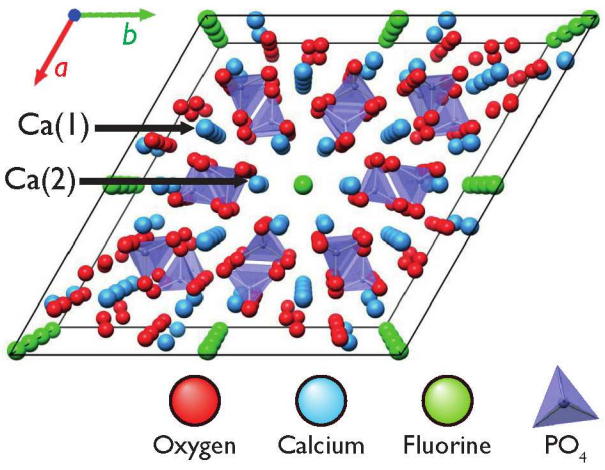

Fig. 1 The fluorapatite structure (viewed down the c axis, [0001]) with the two calcium sites indicated on the figure.

2 Methodology

A classical Born-Mayer description of the crystal lattice has been used[23]. Long range electrostatic interactions between ions were calculated using an Ewald sum[24], in particular the smooth particle mesh variant[25], as implemented in the DL_POLY code was used[26,27]. Short range interactions were described using the Buckingham potential, whereby two ions i and j, separated by a distance r_{ij} , interact with an energy of Φ_{ij} given by[28],

$$\Phi_{ij}(r_{ij}) = A_{ij}\exp\left(\frac{-r_{ij}}{\rho_{ij}}\right) - \frac{C_{ij}}{r_{ij}^6} \qquad (1)$$

where, A_{ij}, ρ_{ij} and C_{ij} are empirically derived parameters[28], specific to pairs of interacting species. The Buckingham potentials were summed within a cut-off value of 10.5 Å, beyond which short range interactions were considered to be negligible.

The potential parameters used in this work are based on those originally reported by Mkhonto and DeLeeuw[29], with the F–F and F–Ca potentials modified by Michie *et al.*[30]. Further modifications in the manner described by Jones *et al.*[31] were required to enable a better description of the PO_4 group in damage situations. Its coefficients for FAp are reported in table 1.

Whilst the Buckingham potentials provide a good description of the atomic forces acting around equilibrium separations, the high energies associated with the simulated collision

Table 1 The modified Buckingham potential parameters for FAp, based on the work of Mkhonto and DeLeeuw[29].

Interaction			A_{ij} (eV)	ρ_{ij}(Å)	C_{ij} (eV Å^6)
$O^{1.045-}$	-	$P^{1.18+}$	610.83	0.2458	0.00
$Ca^{2.00+}$	-	$O^{-1.045-}$	2036.07	0.2883	0.00
$O^{1.045-}$	-	$O^{1.045-}$	22764.30	0.1490	27.89
$F^{1.00-}$	-	$F^{1.00-}$	1317.50	0.2753	13.80
$Ca^{2.00+}$	-	$F^{1.00-}$	1534.30	0.2893	0.00
$O^{1.045-}$	-	$F^{1.00-}$	583833.00	0.2119	7.68

Table 2 The range of ionic separations over which the splines linking ZBL and Buckingham potential forms act.

Interaction			Ionic separation for spline (Å)		
O	-	O	0.558	-	1.000
Ca	-	F	0.100	-	0.300
F	-	F	0.550	-	1.350

cascades lead to atoms coming into close proximity. Within this region the screened nuclear repulsion represented by the Ziegler, Biersack and Littmark (ZBL) potential form provides a better description of the very short range interactions experienced during these high energy collisions[32]. So that both regimes were well described the ZBL and Buckingham potential forms were combined; a smooth transition between the two was provided by an exponential spline whose coefficients were chosen in order that the overall potential was continuous in its first and second derivatives with respect to r_{ij}. The ranges over which the interpolating splines act for each interaction are given in table 2. This potential model has been used successfully to describe the apatite system, in particular it was used recently to predict migration pathways in fluorapatite[14] and chlorapatite using molecular dynamics[15]. In both cases, the activation energy of migration predicted within these studies were found to be consistent with the available experimental data. This is significant here as a correct description of ion transport is important when predicting the recovery of the lattice following radiation damage.

Within MD, Newton's second law of motion is integrated as a function of time[33–35]. From the force description provided by the potential model described above, this allows the time evolution of the positions and velocities of a set of atoms to be calculated. The cascades considered here simulate the effect of an α-decay recoil nucleus. Using MD, radiation damage is simulated by choosing an atom to be the PKA and giving it a kinetic energy in the range of 0.25 to 5 keV in a specific crystallographic direction. The MD algorithm is then run and the time evolution of any damage can be observed through the position of the atoms within the simulation box as the energetic particle interacts with the rest of the system.

A 20×20×20 supercell of FAp containing 336,000 atoms, with cell lengths $a = b = 188$ Å and c=138 Å and the standard apatite cell angles of $\alpha = \beta = 90^\circ$ and $\gamma = 120^\circ$. The simulation cell was initially equilibrated at 300 K for 20 ps in the NVT ensemble (where the temperature and volume remain constant) using a Berendsen thermostat[36]. PKA simulations were then initiated within the NVE ensemble to avoid unwanted scaling of the energetic PKA's velocity by the thermostat and the progress of each displacement cascade was monitored over the course of a 30 ps MD run. This was determined to be enough to capture the short-term phenomena following the cascades, as well as the formation of defects.

Initial runs were performed in order to ensure that the simulation size was sufficient to ensure that the cascade did not overlap with itself across periodic boundaries, even for the 5 keV PKAs. Some test runs were also performed to ensure that 30 ps was adequate and did not prevent major phenomena to be observed.

3 Results and Discussion

3.1 Threshold Displacement Energies

The threshold displacement energy (E_d), is an important physical parameter for understanding and describing radiation damage in crystal structures[37–39]. E_d is the minimum kinetic energy an atom requires to be permanently displaced from its lattice site to another low energy position within the structure, thereby creating a stable defect such as a Frenkel pair. The Kinchin-Pease model[19,40] provides an estimate of the number of atoms displaced permanently (N) from their lattice sites as a function of PKA energy (E),

$$N(E) = \begin{cases} 0, & 0 < P < E_d \\ 1, & E_d < P < 2E_d \\ \frac{E}{2E_d}, & 2E_d < E < E_c \\ \frac{E_c}{2E_d}, & E \geq E_c \end{cases} \quad (2)$$

The general trend in defect numbers predicted by these equations is illustrated in figure 2; once the PKA energy is above $2E_d$ the number of defects formed increases linearly in proportion to $^1/_{2\,E_d}$ until the threshold energy for electronic stopping (E_c) is reached, above which no further lattice defects are assumed to form.

In this work seven low index directions, $\langle 0001 \rangle$, $\langle \bar{1}2\bar{1}0 \rangle$, $\langle \bar{1}2\bar{1}3 \rangle$, $\langle 2\bar{1}\bar{1}0 \rangle$, $\langle 2\bar{1}\bar{1}1 \rangle$, $\langle 11\bar{2}0 \rangle$, $\langle 11\bar{2}1 \rangle$, have been chosen in which to initiate PKAs and therefore predict a direction dependence of E_d for FAp. For each direction and each atom

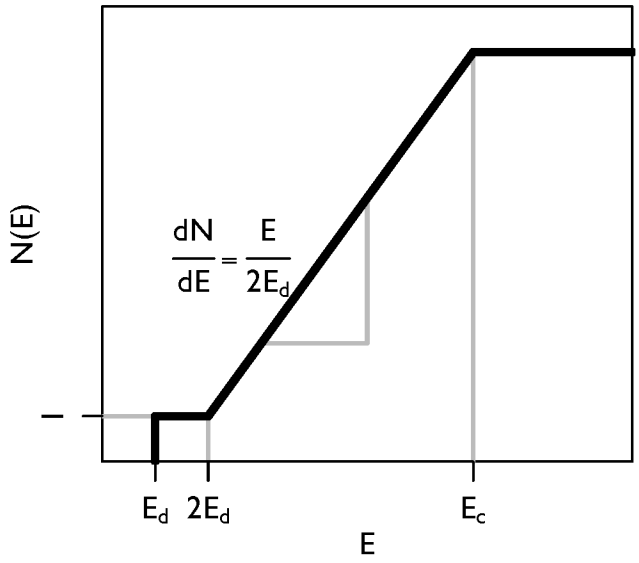

Fig. 2 Graphical representation of the Kinchin-Pease model relating number of displaced atoms, N, to energy of PKA (E). E_d is the threshold displacement energy at which an atom moves permanently off its site, giving rise to a single Frenkel pair, E_c is the value above which electronic stopping will occur and the gradient of the line is $\frac{P}{2E_d}$.

type, the determination of E_d has been done using a method described by Robinson *et al.*[41]. In this method, 5 PKAs are set in motion for each combination of direction and atom type using a range of energies. The probability $P(E)$ of PKA displacement for a particular energy is given as the number of simulations performed for that energy divided by the number of simulations in which the PKA was permanently displaced from its initial site. The threshold displacement energy is then the energy at which this probability is equal to $1/2$, with an associated uncertainty δE_d. In this work, it is defined such that the probability $P(E - \delta E_d) < 0.05$ and $P(E + \delta E_d) > 0.95$. Values for the uncertainty δE_d are typically between 4 and 20 eV in our simulations. In general, the distribution of E_d depends on the temperature. These simulations were run at the same temperature as the displacement cascades (300 K).

Table 3 reports E_d values for all directions and species. Interestingly the anions exhibit lower E_d values than the cations. This correlates with defect energies required to remove the species from the lattice calculated using Mott-Littleton methodology[42]; 4.9 eV for F, 9.9 eV for O, 30.4 eV for P and 22.1 eV for Ca(1) and 22.8 eV for Ca(2).

3.2 Collision Cascades

The E_d calculations described in the previous section aim to characterise localised displacement events typically leading to the formation of a single Frenkel pair. As a consequence the energy given to the PKA in such simulations is relatively low. Increasing the energy into the keV range promotes the simulation of entire collision cascades, inducing defects in extended volumes of the lattice. Here, cascade simulations were performed for two directions, $\langle 2\bar{1}\bar{1}0\rangle$ and $\langle 0001\rangle$, as these exhibited the highest and lowest E_d values respectively (as reported in table 3). A range of energies were used in each direction: 0.25, 0.5, 0.75, 1, 2, 3, 4 and 5 keV and in each case a Ca(1) atom was used as the PKA initiating the cascade.

In order to compare the results of the collision cascades with predictions made using the Kinchin-Pease model, it is necessary to count the maximum number of point defects occurring within the simulation box over the course of the MD run. In order to achieve this, the atom positions within the damaged material were compared with the positions of sites in the perfect lattice as the simulation proceeded. Defects were identified using a distance cut-off method[17,43]: a cut-off of 0.8 Å was employed. Any atom more than the cut-off distance from a lattice site was counted as an interstitial. Similarly, any perfect lattice site without atoms within its cut-off indicated the presence of a vacancy. If an ion recombined with a vacant lattice site, whose type was different to that in the perfect lattice, this was classified as a substitutional defect. Recombination with a homogeneous site did not yield a defect as this constitutes lattice recovery (even if the atom did not originally occupy that site).

Using the method described above, numbers of defects and recovery profiles were calculated as a function of time. Figures 3(a) and 3(b), present the general pattern for damage and recovery for each PKA energy in the $\langle 0001\rangle$ and $\langle 2\bar{1}\bar{1}0\rangle$ directions respectively. After maximum damage is reached, the lattice immediately starts to recover, although some retained damage is exhibited at the end of the simulation, suggesting recovery is incomplete on the timescales considered. This effect has also been observed experimentally by Afra *et al.*[44]. Interestingly, for damage cascades in the $\langle 0001\rangle$ direction, the overall percentage recovery of FAp after damage averages 70 % (compared with 64 % for the $\langle 2\bar{1}\bar{1}0\rangle$ direction) across all energies.

Results for both sets of directions described in figures 3(a) and 3(b), show that the total number of defects produced increases linearly with the energy given to the PKA, which is in agreement with the Kinchin-Pease model[19]. It is also clear that the direction in which the PKA is initiated makes a difference to the total number of defects. Figure 4 shows that for 5 keV cascades, there is an increase in defect population of ~25% from the $\langle 2\bar{1}\bar{1}0\rangle$ to $\langle 0001\rangle$ directions. This can be related back to the threshold displacement trends for FAp reported previously in table 3. The second hump shown for the $\langle 0001\rangle$ cascade correlates to a secondary cascade in the damaged region.

	⟨0001⟩	⟨$\bar{1}2\bar{1}0$⟩	⟨$\bar{1}2\bar{1}3$⟩	⟨$2\bar{1}\bar{1}0$⟩	⟨$2\bar{1}\bar{1}1$⟩	⟨$11\bar{2}0$⟩	⟨$11\bar{2}1$⟩
Ca(1)	**39** ± **7**	57 ± 6	50 ± 5	73 ± 5	70 ± 10	62 ± 7	75 ± 8
Ca(2)	**48** ± **8**	104± 6	**53** ± **9**	62 ± 8	56 ± 10	84 ± 6	100± 11
F	**9** ± **2**	37 ± 3	22 ± 4	90 ± 10	19 ± 8	16 ± 4	31 ± 9
O	**15** ± **3**	39 ± 5	19 ± 7	21 ± 2	16 ± 6	28 ± 7	**16** ± **5**
P	22 ± 4	19 ± 5	19 ± 7	52 ± 9	15 ± 2	48 ± 8	**10** ± **2**

Table 3 Calculated threshold displacement energy ranges (in eV) for FAp in the hexagonal directions indicated. The lowest energies are shown in bold, for each ion type.

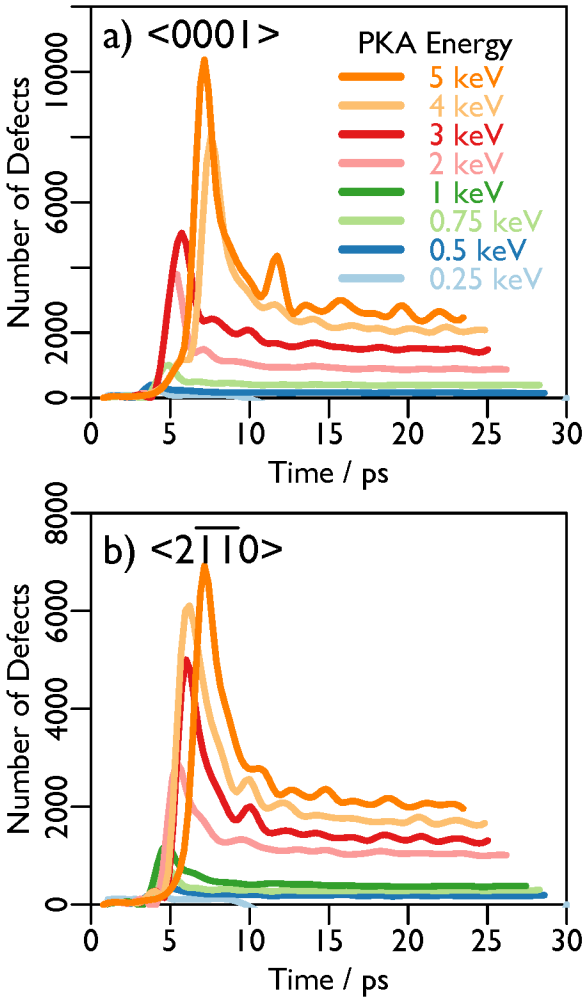

Fig. 3 Number of displaced atoms as a function of simulation time for the PKA energies considered: a) PKA initiated in ⟨0001⟩, b) ⟨$2\bar{1}\bar{1}0$⟩ directions.

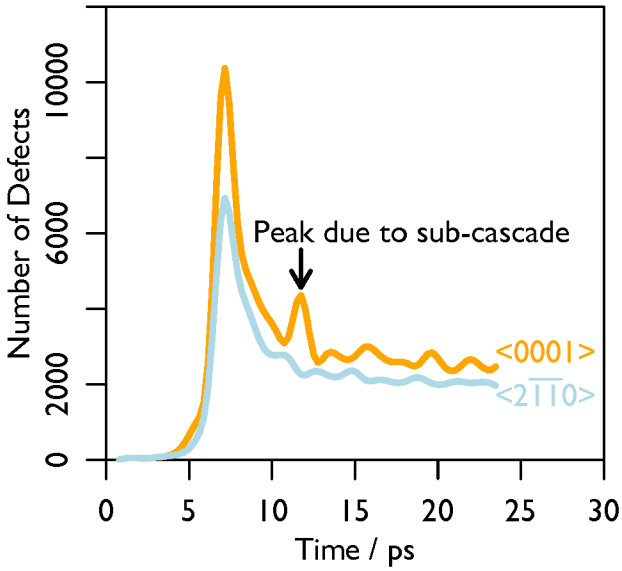

Fig. 4 Comparison of total number of defects for 5 keV cascades in both directions.

Figures 5(a) and 5(b) show the maximum isolated defect counts for each cascade as a function of PKA energy. Due to the stoichiometry of the system, there are different numbers of each element within the simulation box. Thus, in order to gauge if a particular species is disproportionately affected by a cascade, defects counts have been normalised to the total number of atoms of that type within the system and expressed as a percentage.

A comparison of these normalised defect populations shows a greater number of anion defects than cation defects. Furthermore, they are in good agreement, for both number and type of defect predicted from the E_d values in table 3 in conjunction with the Kinchin-Pease method. This suggests that, notwithstanding the complexity of the apatite structure, the relatively simple Kinchin-Pease model provides a reasonable way for obtaining predictions of the defect population following radiation damage within this system[19].

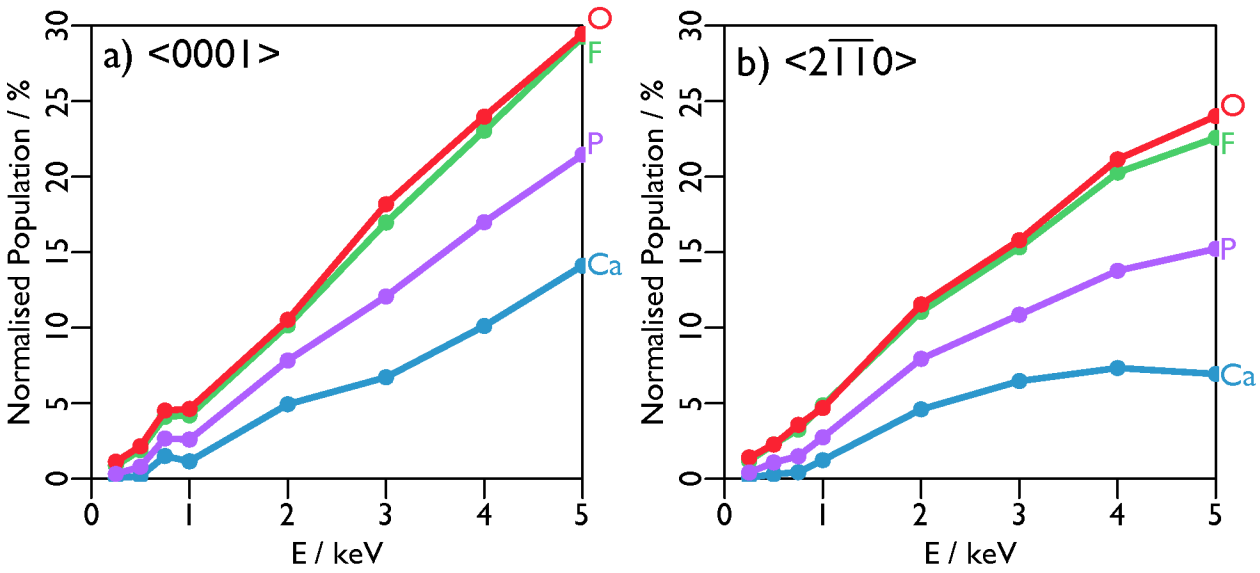

Fig. 5 Total number of defects created for each species expressed as percentage of total number each element in simulation box as a function of PKA energy for a) $\langle 0001 \rangle$ and b) $\langle 2\bar{1}\bar{1}0 \rangle$ directions.

3.3 Phosphate polyhedra

The phosphate tetrahedra within FAp represent a fundamental building block of the structure. When monitoring damage within a cascade it is therefore useful, to consider these tetrahedra, not simply as one phosphate atom and four oxygen atoms, but rather as a single structural unit. A good example of this is given by White *et al.*[21] and Madhavi *et al.*[45] who discuss how the PO_4 tetrahedra and the Ca meta-prisms, move and twist in order to accommodate changes to the lattice.

Within this process, the geometry of the PO_4 tetrahedra remains, essentially unchanged, with the rotation of connected units facilitating structural changes. Given their significance the damage and recovery processes affecting these phosphate units themselves and their correspondence to each other, is important in understanding FAp's radiation tolerance. As a result, specific attention has been given to the phosphate polyhedra and their structural evolution over the course of a radiation damage cascade.

Before considering how the topology of the apatite structure was affected by the cascades, damage to the individual PO_4 polyhedra was examined by calculating the coordination number of each phosphorus atom (denoted as n). Using a simple distance cut-off scheme the number of oxygen ions surrounding each phosphorous atom was counted as each cascade progressed: an oxygen and a phosphorus atom are neighbours if the distance between them is shorter than 1.9 Å. This distance was chosen based on the FAp equilibrium P-O bond length of 1.61 Å, calculated from the P-O pair-correlation function obtained from a 300K MD simulation of the perfect lattice. The cut-off was extended beyond this value by 20% in order to capture the atoms that deviate from this average distance because of thermal vibration and possible nearby defects, thus, the atoms that have an anomalous local environment can be characterised depending on their co-ordination number.

The immediate result of the coordination analysis, performed on the final configuration of the displacement cascade has been used to visualise the core of the damaged region in figure 6. In this picture, only the O and P atoms that have an anomalous coordination number are visible, as well as their neighbours, to improve clarity. This analysis can be carried out for successive snapshots of a simulation, thus revealing the evolution of the population of atoms in each different coordination state, as shown figure 7 for a 1 keV cascade along a $\langle 0001 \rangle$ direction.

The coordination number of the P ions calculated this way provides information on damage to PO_x polyhedra. In the undamaged structure PO_4 tetrahedra are expected, however a cascade may result in the formation of over, or under-coordinated P atoms. Indeed, figure 7(a) shows that early in the cascade defect polyhedra with coordination numbers of 2, 3, 5 and 6 are formed. After 2 ps, the production of 2-coordinated P stops, and their number drops rapidly to zero. Shortly thereafter the same thing happens for the 3-coordinated P species. This behaviour is qualitatively different for 5 coordinated P atoms whose population stops growing but subsequently remains relatively constant. The number of n=1 and n=6 P ions remains very low throughout and furthermore no coordination number greater than 6 was observed. After

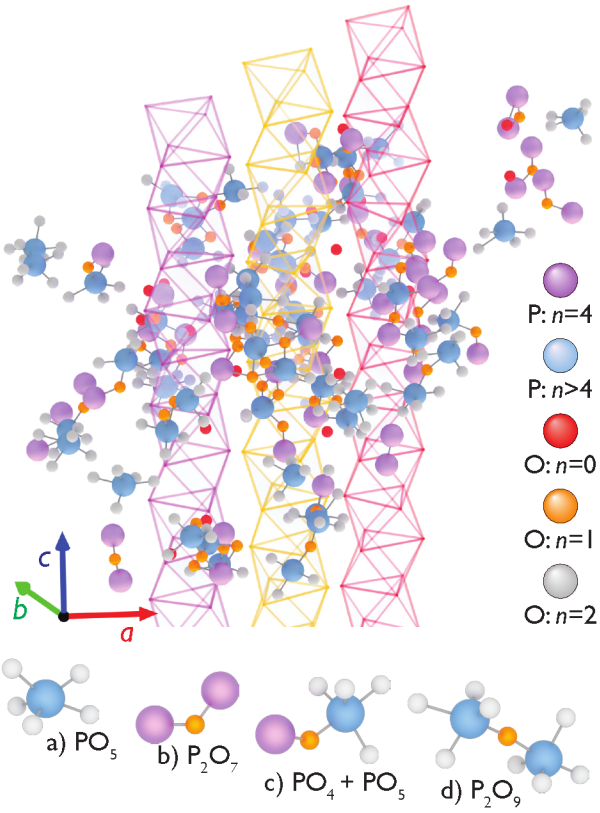

Fig. 6 Damage after a displacement cascade: P and O atoms with imperfect coordination number and their first neighbours are represented. Details of the most common structures are inset: (a) a PO_5 unit, (b) two linked PO_4 (P_2O_7 dimer), (c) one PO_4 linked with a PO_5 (P_2O_8 chain), (d) two PO_5 (P_2O_9 dimer). To allow comparison, and to provide better context, the viewing direction and colour coded calcium meta-prisms are the same as used in figure 10.

6ps the number of each kind of defect is stable remaining effectively constant until the end of the simulations at 25 ps.

This indicates that while the PO_x polyhedra with $x < 4$ are unstable and recombine with O atoms, PO_5 units are more stable. Over the times considered in this study, the PO_5 population fluctuates around an average value after ~6 ps without a clear decrease. Whether they remain as PO_5 over longer timescales or split into PO_4 + O is still unknown. This means that some P atoms have a local environment significantly different from that in the perfect crystal.

This behaviour is qualitatively similar for both 1 keV and 5 keV cascades. The effect of increased energy being a higher number of defects, but the initial peaks of under-coordinated P and O remains, along with the almost constant number of 5-coordinated P and bridging oxygens after the initial increase. The initial direction of the PKA does not change the qualitative behaviour either, the difference between the $\langle 0001 \rangle$ and $\langle 2\bar{1}\bar{1}0 \rangle$ cascades being only a small change in the number of defects.

3.4 Bridging oxygens

Another kind of damage, relevant to the phosphate units, relates to how they are organised. In the perfect crystal, the phosphate tetrahedra are not directly connected to one another. As they neither share edges nor corners each O atom is only associated with a single P atom (n=1). Using the same cut-off as before, the number of P atoms coordinating each O atom was calculated and has been plotted in figure 7(b) (note: within the plot only defective oxygens, where $n \neq 1$ are considered). During the initial damage phase there is a rapid increase in the number of zero and two-coordinated oxygen atoms, this reaches a maximum at about 1.8 ps.

Although both curves show evidence of recovery, with the population of defects decreasing following peak damage, the n=0 trace decreases much more rapidly. By comparison the n=2 curve shows a step down at about 4 ps before remaining somewhat constant for the remainder of the simulation.

Oxygen atoms with n=2 are in a bridging configuration, linking two phosphorus atoms. Their presence during a cascade is indicative of polymerisation of the phosphate substructure. The result of forming a bridging oxygen is to release another oxygen from its initial tetrahedron ($2\ PO_4 \rightarrow P_4O_7$+O) which can then be integrated into a phosphate tetrahedron, contributing to PO_5 polyhedra that then contribute to the P_2O_8 and P_2O_9 dimers shown in figure 6. The n=0 oxygens are oxygens emitted during this polymerisation process that do not recombine with a phosphorus (henceforth referred to as "free" oxygen).

The environment of the "free" oyxgens is illustrated in figure 8 which shows the correlation function for "free" oxygen-phosphorous pairs (figure 8a) and calcium pairs (figure 8b).

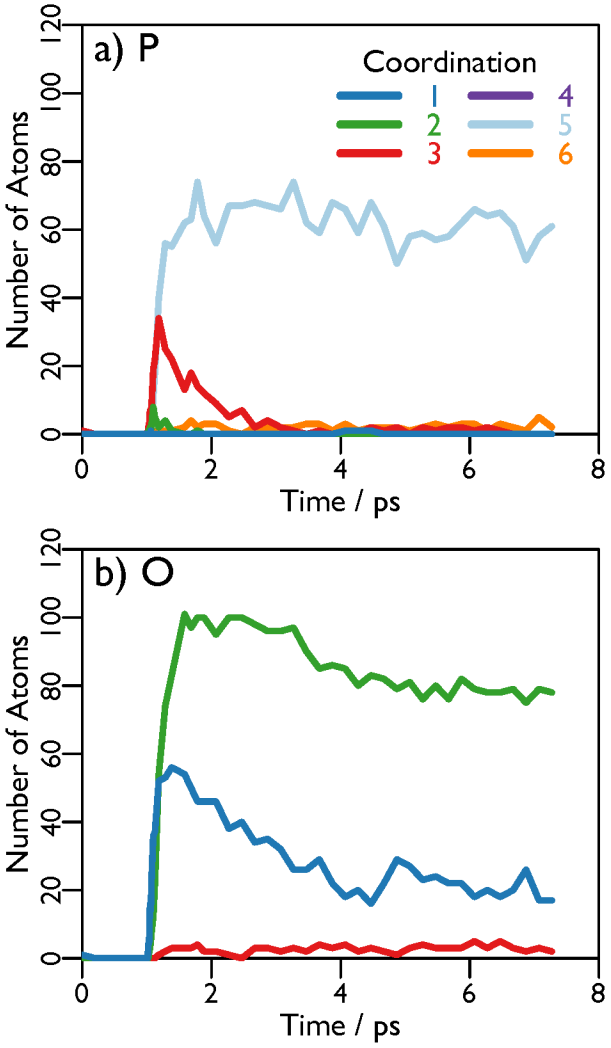

Fig. 7 Evolution of atom populations for different coordination numbers n given as functions of time during the beginning of a displacement cascade simulation. Atoms with the coordination number of the perfect structure are omitted (1 for O and 4 for P).

Unlike lattice oxygen, the "free" oxygen is not coordinated by phosphorous (figure 8a). By comparison, the pair-correlation with Ca shows that some form of order is retained, as the first peak around 2.2 Å is consistent with that found in the perfect crystal. This indicates that the oxygens sitting outside phosphate polyhedra are associated with calcium atoms possibly in a charge-compensating role.

3.5 Phosphate chains

Further analysis of the damaged phosphate sub-structure is done by calculating the distribution of the different chain lengths N (i.e. the number of polyhedra that are part of a given chain). The results of this analysis are shown in figure 9.

A chain length of one corresponds to an unconnected polyhedron/monomer PO_x, where x is either 4 or 5. Initially, their number is equal to the number of phosphorus atoms. As the cascade develops, the curve in figure 9 shows a large initial dip, reaching a minimum at ~2 ps before recovering slightly to form a plateau from 5 ps to the end of the simulation. Concomitant with the decrease in the monomer count is the formation of phosphate chains. Although chains with lengths of up to seven PO_x units were detected, these only accounted for a very small proportion of the polymerised phosphate content. Rather, following peak damage, the majority of linked PO_x were found in the N=2 configuration (dimers, or P_2O_y chains), with smaller but still appreciable numbers of N=3, N=4 and even N=5 chains being retained at the end of the simulation. The damage plume resulting from the cascade in figure 6 shows how these various PO_x chains relate to each other. Most of the defects identified were PO_5 units, and P_2O_y chains, y being 7, 8 or 9. A number of bridging oxygens are also clearly visible (n=2), together with some "free" oxygens (n=0).

The same simulations were done for higher energy cascades (5 keV), along $\langle 0001 \rangle$ and $\langle 2\bar{1}\bar{1}0 \rangle$ directions. The number of defects during these cascades are shown on figure 11; from a qualitative point of view, all the features form the lower-energy cascades are still present, namely the initial peak in the number of free oxygens followed by a sharp decline and a stabilisation, as well as a high number of both five-coordinated P and bridging oxygens throughout the simulation. Moreover, except for a slightly higher number of defects in the case of the $\langle 0001 \rangle$ cascade, both directions exhibit very similar behaviour.

The simulations suggest that, during the course of a displacement cascade, most damage is sustained by phosphate sub-structure. The number of defective Ca was found to be statistically insignificant with any damage to the Ca metaprisms recovering in less than a picosecond. Similarly, the F ions remained contained in the channels in all cases. The phosphate substructure showed notable changes, with displaced O and P atoms rearranging to form a glass-like, poly-

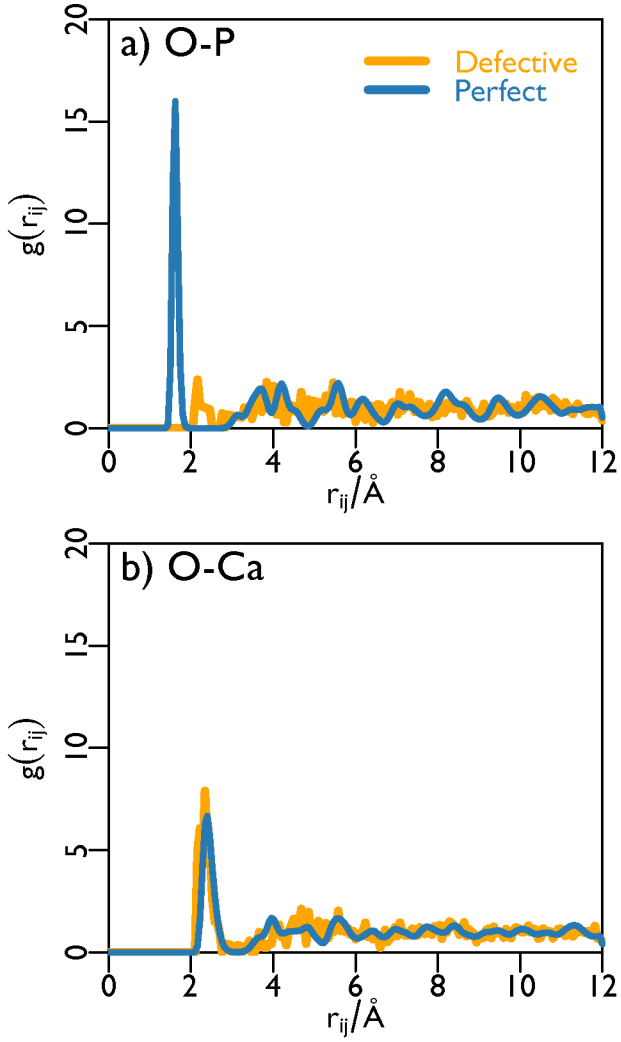

Fig. 8 Partial pair correlation functions calculated around "free" oxygen atoms (i.e. those that are not part of any PO_x polyhedron and have $n = 0$) calculated after a displacement cascade (defective) in comparison to perfect crystal for (a) O-P and (b) O-Ca correlation functions.

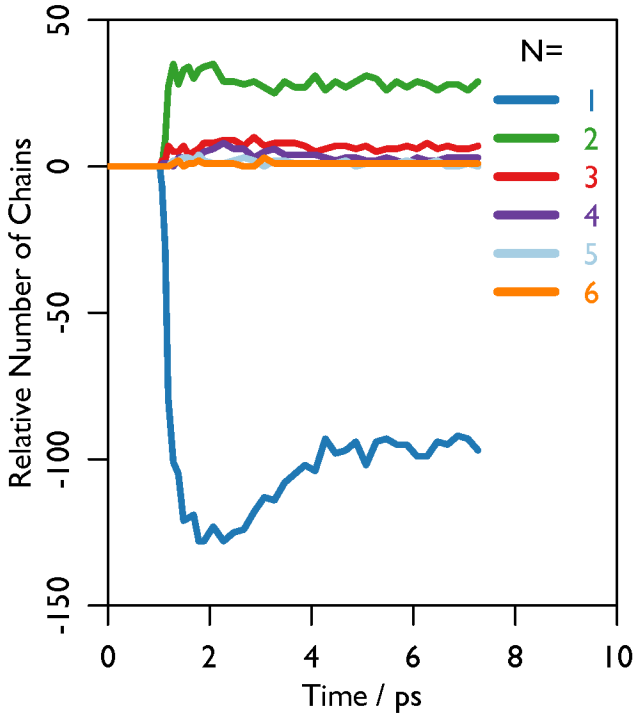

Fig. 9 Number of PO_x polyhedra chains with different chain lengths given over the course of a displacement cascade.

merised structure intertwined with the meta-prisms.

Whilst the overall number of defects from both methods is significant, the simple distance scheme tends to detect more defects than the polyhedra analysis. For example, if one tetrahedron rotates and moves slightly, all its 5 atoms will be counted as defects in the first case, whereas the second method will still recognise it as a tetrahedron.

4 Conclusions

This work has shown that the threshold displacement energies for FAp are directional and that the anions in this system exhibit the lowest threshold energies. This is also seen in the normalised defect population produced from damage cascades. Additionally, damage introduced into the FAp system recovers by ~70% over the MD timescale considered here (20 to 30 ps).

Importantly, although counting individual defects provides information about the type of damage that might be expected in a cascade, it does help to understand the effect on the PO_4 structural units and not their association with one another. Therefore, we have described an approach for identifying the structural damage of these units by considering the change in nearest neighbours and their polymerisation. This shows that although many PO_4 groups may move or rotate from their

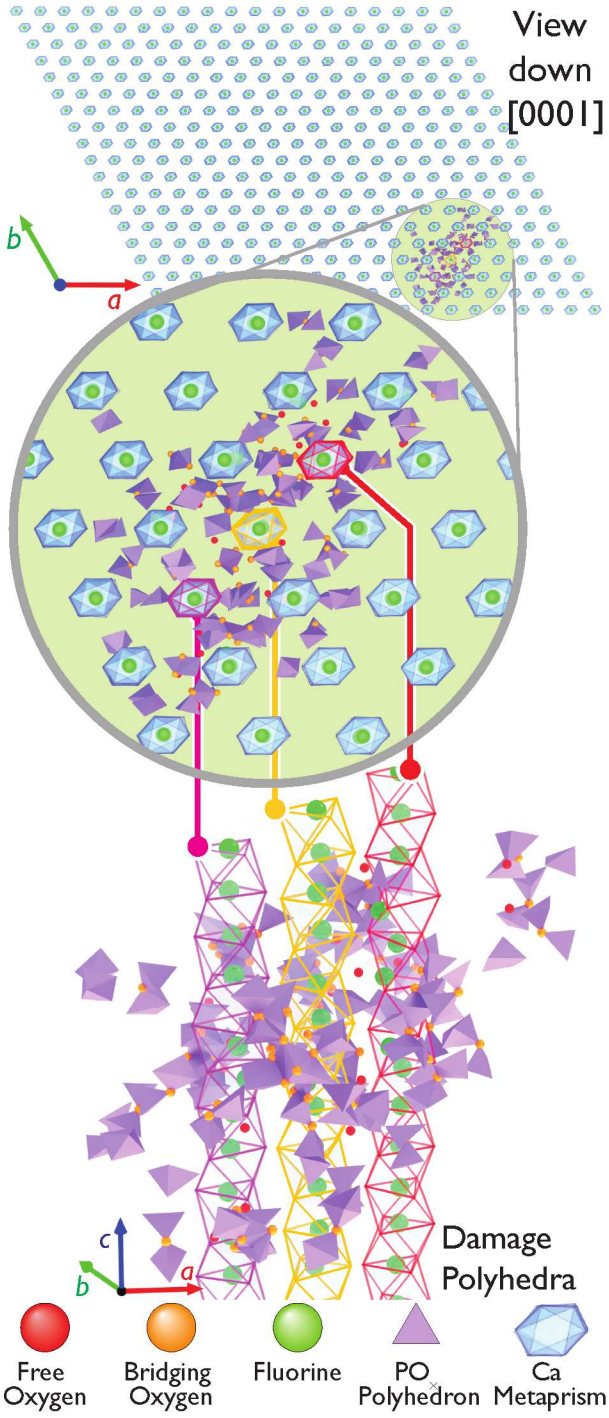

Fig. 10 Damage after a displacement cascade. For clarity only the the damage is shown in addition to Ca(2) meta-prisms and fluorine ions. The top image the damage in the context of the simulation cell, down the [0001] direction. The middle and bottom images are more detailed views of the defects resulting from the cascade. They show how the phosphate defects are distributed around the meta-prisms (the coloured channels are the same in both the middle and bottom images).

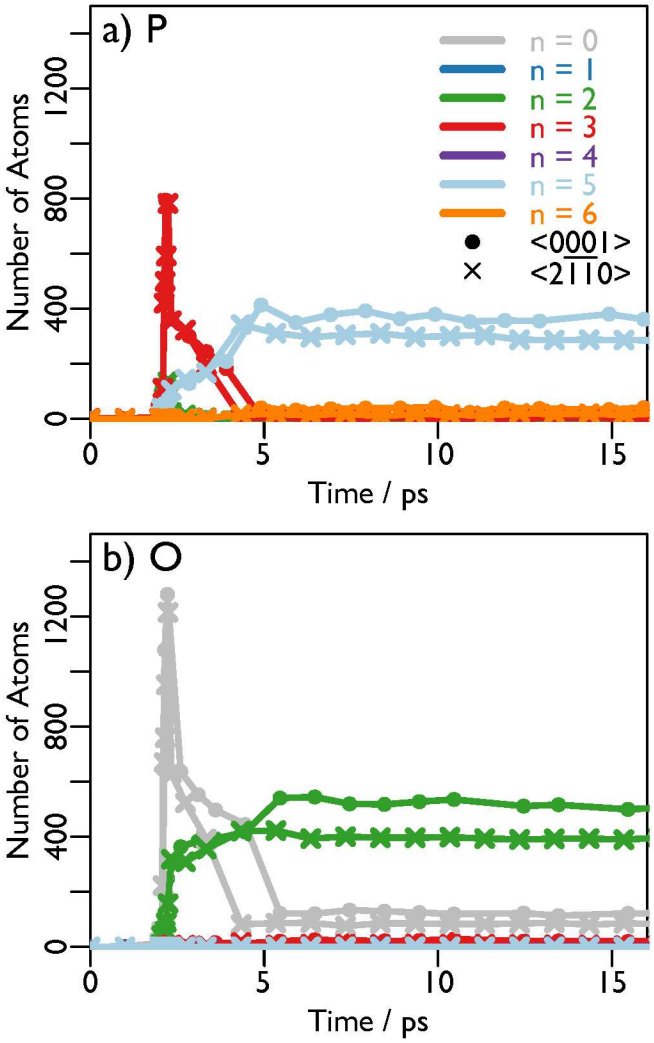

Fig. 11 Atom populations for different coordination numbers n as functions of time during 5 keV displacement cascades in the $\langle 0001 \rangle$ (circles) and $\langle 2\bar{1}\bar{1}0 \rangle$ (crosses) directions: (a) P ions; (b) O ions. The atoms having the coordination numbers of the perfect structure (1 for O and 4 for P) are omitted.

original lattice positions during damage events, a large proportion are retained intact.

Within the core of the damaged region, however, PO_x units are found to form chain like structures. Interestingly, the fluorine channels and the Ca meta-prisms that describe them are relatively unperturbed, with defective PO_x chains threading between them. It shows that in this material, displacement cascades have very different effects on the channels and the phosphate structure. Overall, the calcium meta-prisms are more radiation-tolerant than other features of the crystal. Because of that, the fluorine ions tend to remain contained in the channels, although they have low displacement threshold energies and a high defect relative population. The glass-like structure of the phosphate defects underlines the importance of considering both individual defects and larger structural units when studying damage events in this structure.

5 Acknowledgments

EEJ acknowledges AWE for financial support and Brian Metcalfe, Shirley Fong and Philip Mallinson for useful discussions. Computing resources were provided by the Imperial College High Performance Computing Service; (http://www.imperial.ac.uk/ict/services/teachingandresearchservices/highperformancecomputing).

References

1 J. M. Hughes and J. Rakovan, *Rev. Mineral. Geochem.*, 2002, **48**, 1–12.
2 Y. Pana and M. E. Fleet, *Rev. Mineral. Geochem.*, 2002, **48**, 13–50.
3 A. Chroneos, R. V. Vovk and I. L. Goulatis, *Montash. Chem.*, 2011, **143**, 345–353.
4 W. Lutze and R. C. Ewing, *Radioactive Waste Forms for the Future*, North-Holland, Amsterdam, 1988.
5 C. Ewing. R and L. Wang, *Rev. Mineral. Geochem.*, 2002, **48**, 673–699.
6 A. E. Ringwood, S. E. Kesson, N. G. Ware, W. Hibberson and A. Major, *Nature*, 1979, **278**, 219–223.
7 I. W. Donald, B. L. Metcalfe and R. N. J. Taylor, *J. Mat. Sci.*, 1997, **32**, 5851–5887.
8 I. W. Donald, *Waste Immobilization in Glass and Ceramic Based Hosts*, John Wiley & Sons, Ltd, Chichester, UK, 2010.
9 A. J. Gleadow, D. X. Belton, B. P. Kohn and R. W. Brown, *Rev. Mineral. Geochem.*, 2002, **48**, 579–630.
10 R. Fleischer and P. Price, *Geochim. Cosmochim. Ac.*, 1964, **28**, 1705–1714.
11 R. A. Ketcham, A. Carter, R. A. Donelick, J. Barbarand and A. J. Hurford, *Am. Mineral.*, 2007, **92**, 799–810.
12 I. Donald, B. Metcalfe, S. Fong, L. Gerrard, D. Strachan and R. Scheele, *J. Nucl. Mater.*, 2007, **361**, 78–93.
13 S. K. Fong, I. Donald and B. L. Metcalfe, *J. Alloy. Compd.*, 2007, **444-445**, 424–428.
14 E. E. Jay, M. J. D. Rushton and R. W. Grimes, *J. Mater. Chem.*, 2012, **22**, 6097–6103.
15 M. L. Jackson, E. E. Jay, M. J. D. Rushton and R. W. Grimes, *J. Mater. Chem. A*, 2014, **2**, 16157–16164.
16 W. J. Weber, R. C. Ewing, C. R. A. Catlow, T. D. de la Rubia, L. W. Hobbs, C. Kinoshita, H. Matzke, A. T. Motta, M. Nastasi, E. K. H. Salje, E. R. Vance and S. J. Zinkle, *J. Mater. Res.*, 1998, **13**, 1434–1484.
17 L. Veiller, J. Crocombette and D. Ghaleb, *J. Nucl. Mater.*, 2002, **306**, 61–72.
18 B. T. Kelly, *Irradiation damage to solids*, Pergamon Press, 1966, p. 232.
19 G. H. Kinchin and R. S. Pease, *Rep. Prog. Phys.*, 1955, **18**, 1–51.
20 J. O. Nriagu and P. B. Moore, *Phosphate Materials*, Springer-Verlag Berlin Heidelberg New York Tokyo, 1st edn, 1984.
21 T. White and D. ZhiLi, *Acta Crystallogr. B*, 2003, **59**, 1–16.
22 B. Beevers and D. McIntyre, *Mineral. Mag.*, 1946, **27**, 254–259.
23 M. Born and J. Mayer, *Z. Phys.*, 1932, **75**, 1–18.
24 P. Ewald, *Ann. Phys.*, 1921, **369**, 253–287.
25 U. Essmann, L. Perera, M. L. Berkowitz, T. Darden, H. Lee and L. G. Pedersen, *J. Chem. Phys.*, 1995, **103**, 8577.
26 W. Smith and I. T. Todorov, *Mol. Simulat.*, 2006, **32**, 935–943.
27 W. Smith and T. R. Forester, *J. Mol. Graph.*, 1996, **14**, 136.
28 R. A. Buckingham, *Proc. R. Soc. Lond. A.*, 1938, **168**, 264.
29 N. H. de Leeuw and J. A. L. Rabone, *Cryst. Eng. Comm.*, 2007, **9**, 1178.
30 E. M. Michie, R. W. Grimes, S. K. Fong and B. L. Metcalfe, *J. Solid State Chem.*, 2008, **181**, 3287–3293.
31 A. Jones, P. R. Slater and M. S. Islam, *Chem. Mater.*, 2008, **20**, 5055–5060.
32 J. F. Ziegler, J. P. Biersack and U. Littmark, *The Stopping and Range of Ions in Solids, vol. I*, Pergamon, 1985.
33 D. C. Rapaport, *The art of molecular dynamics simulation*, Cambridge University Press, 2004, p. 549.
34 M. P. Allen and D. J. Tildesley, *Computer Simulation of Liquids*, Oxford University Press, Oxford, 1989.
35 D. Frenkel and B. Smit, *Understanding molecular simulation: from algorithms to applications*, Elsevier, 2002.
36 H. J. C. Berendsen, J. P. M. Postma, W. F. van Gunsteren, A. DiNola and J. R. Haak, *J. Chem. Phys.*, 1984, **81**, 3684–3670.
37 G. Lucas and L. Pizzagalli, *Phys. Rev. B*, 2005, **72**, 161202.
38 B. Liu, H. Y. Xiao, Y. Zhang, D. S. Aidhy and W. J. Weber, *J. Phys.: Condend. Matter*, 2013, **25**, 485003.
39 R. Devanathan and W. J. Weber, *J. Appl. Phys.*, 2005, **98**, 086110.
40 M. Norgett, M. Robinson and I. Torrens, *Nucl. Eng. Des.*, 1975, **33**, 50–54.
41 M. Robinson, N. A. Marks, K. R. Whittle and G. R. Lumpkin, *Phys. Rev. B*, 2012, **85**, 104105.
42 N. F. Mott and M. J. Littleton, *Trans. Faraday Soc*, 1938, **34**, 485–499.
43 J. A. L. Rabone, A. Carter, A. J. Hurford and N. H. Leeuw, *Phys. Chem. Miner.*, 2008, **35**, 583–596.
44 B. Afra, M. Lang, M. Rodriguez, J. Zhang, R. Giulian, N. Kirby, R. Ewing, C. Trautmann, M. Toulemonde and P. Kluth, *Phys. Rev. B*, 2011, **83**, 064116.
45 T. White, C. Ferraris, J. Kim and S. Madhavi, *Rev. Mineral. Geochem.*, 2005, **57**, 307–401.

Radiation Damage in Fluorapatite

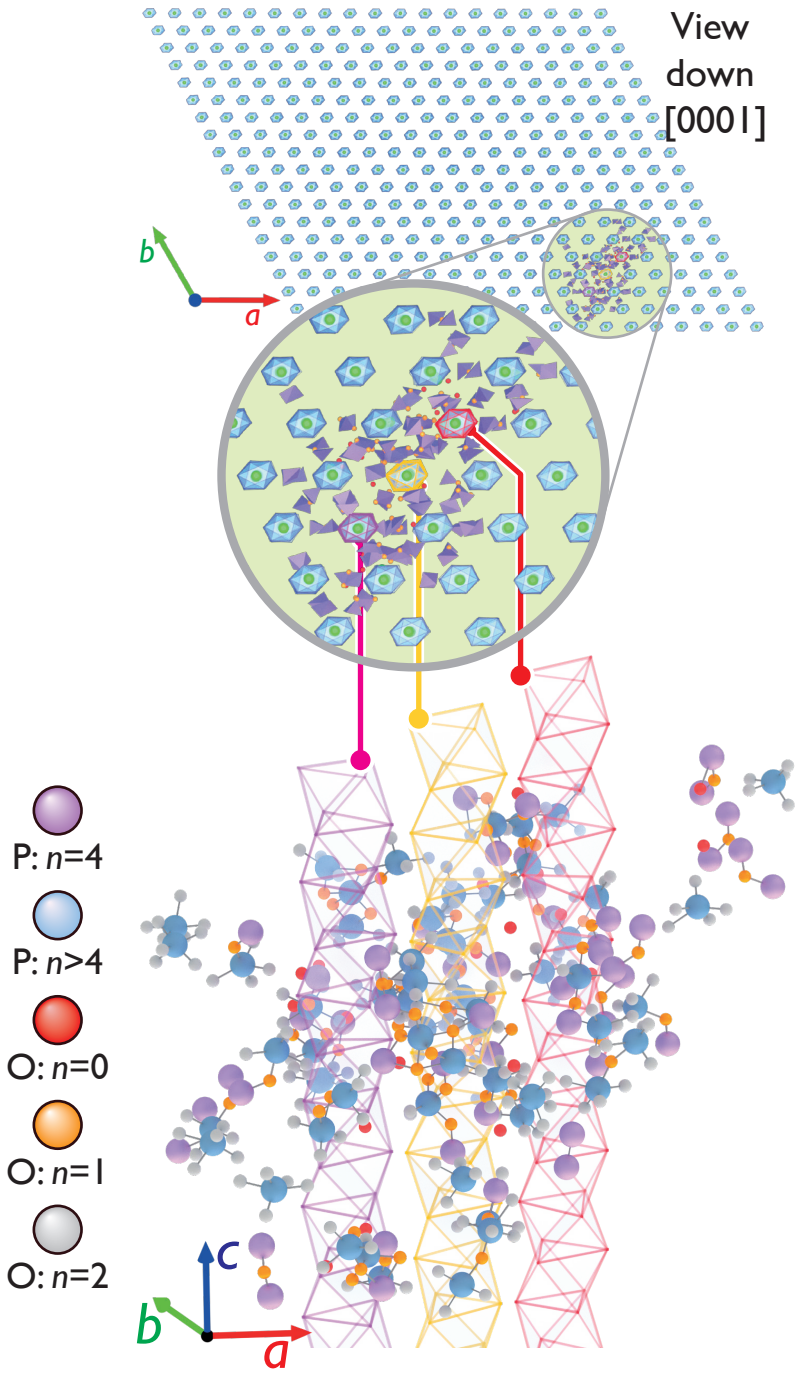

Molecular dynamics simulations, used in conjunction with a set of classical pair potentials, have been employed to examine simulated radiation damage cascades in the fluorapatite structure. Regions of damage have subsequently been assessed for their ability to recover and the effect that damage has on the important structural units defining the crystal structure, namely phosphate tetrahedra and calcium meta-prisms.

The image shows how the coordination environment of phosphorous and oxygen atoms was affected within at the core of the region of the lattice affected by the damage cascade. Atoms whose coordination number (n) is different to that in the perfect lattice are shown. The colour-coded calcium meta-prisms show that these structural units and the fluorine channels they describe were almost wholly unaffected by the damage cascade. By comparison the topology of the phosphate polyhedra in this region was altered, as they polymerised to form chains up to seven units in length. This meant that the damaged region could be characterised as amorphous phosphate chains interlaced with regular features of the original undamaged apatite structure.